Signal-to-Noise Ratio in Heat-Assisted-Recording Media: A Comparison between Simulations and Experiments

Andrea Meo[,1,*] K. Pituso,[2] P. Kampun,[2] K. Pornpitakpong,[2] A. Suntives,[2] S.E. Rannala,[3]
R.W. Chantrell,[3] P. Chureemart,[1] and J. Chureemart[1,†]

[1]*Department of Physics, Mahasarakham University, Mahasarakham 44150, Thailand*
[2]*Seagate Technology, Teparuk, Samutprakarn 10270, Thailand*
[3]*School of Physics, Engineering and Technology, University of York, York YO10 5DD, United Kingdom*

We develop a code to extract the signal-to-noise ratio (SNR) arising from the magnetic film in a recording medium. The approach allows us to separate the remanence and transition contributions from the global spatial noise. The results are in excellent agreement with the analysis performed on the same data sets by means of Seagate proprietary software based on ensemble wave-form analysis. We then apply this analytical approach to the results of heat-assisted magnetic recording (HAMR) dynamics simulations by means of the open-source multi-time-scale micromagnetic code MARS and compare these with experimental spin-stand measurements of analogous systems. The proposed model could be used as the standard tool to understand the underlying physics of the noise components affecting HAMR operations and how to decrease the noise arising from the medium to improve the writing performance of HAMR.

I. INTRODUCTION

The signal-to-noise ratio (SNR) describes how good the readback signal is with respect to the background noise, which might arise from the medium, from the reading process, or from nearby appliances. Variation in the SNR can lead to changes in the bit error rate (BER) and consequently it can affect the areal-density capability of the device [1,2]. This makes it one of the most important parameters of a hard drive and as such it is the object of constant effort aimed to improve it. The SNR for an arbitrary sequence can be determined by a time-domain correlation analysis as $\text{SNR} = 10 \log \text{Var}[V_s(t)]/\text{Var}[V_n(t)]$ [3], where $V_{s,n}(t)$ are the signal and noise components of the readback voltage and Var is the variance. This total spatial SNR in a recording medium can be ascribed to two separate noise components: remanence and transition noise [4,5]. The former is caused by grains within a bit region that either have not been reversed or have switched back after the writing process. As the grain size shrinks to allow for larger areal densities, the thermal stability degrades, favoring this process. These grains reduce the saturation value of the magnetization at remanence and affect the readback signal. It is important to observe that the remanence noise is a low-frequency noise and would be present even in a track where a single bit is written; hence this

noise component will always be present in a recording medium. The latter is a measure of the shift of a recorded transition with respect to the ideal location of the transition. It is generally called jitter and is experimentally defined as the standard deviation of the shift in transition locations [6,7]. Nonetheless, it can be characterized in terms of the SNR. Once the total spatial noise is acquired, it can be decomposed into remanence and transition components by applying appropriate windowing functions to the spatial noise. The ensemble wave-form analysis approach developed by Seagate technology [7,8] allows us to obtain the spatial SNR and extract the remanence and transition components. Our goal is twofold: on the one hand, we aim to be able to perform an analysis of bit sequences to extract SNR components analogous to the aforementioned Seagate method by means of an in-house code. This is motivated by the absence of freely available tools to perform this kind of analysis: only in-house untested and unverified calculators can be found in the literature. On the other, we aim to apply this analysis to demonstrate that the recently developed fully tested open-source package MARS [9] is capable of simulating realistic HAMR media and processes and that it can be useful tool to improve HAMR performance.

II. EXPERIMENTAL DETERMINATION OF SNR

The spin stand is a versatile recording head tester that can test many heads on one medium with very flexible

---
*andrea.m@msu.ac.th; andrea.meo@poliba.it
†jessada.c@msu.ac.th

settings. In this experiment, the spindle speed is 7200 rpm (revolutions per minute) and the recording heads are tested on the middle diameter with a $0°$ skew angle. The active fly clearance target is 1.5 nm with heater power compensation during the laser-current sweeps. The maximum areal-density capability is measured for the optimal write current. For the laser current, we first run the same algorithm of the magnetic field strength measurement [10] to obtain the Curie current, which produces the heat equivalent to the Curie temperature. The laser currents in the SNR experiment are varied as the ratio of the Curie current, which can be converted into the writing temperature. We use a 10×10^9 samples/s spin-stand built-in digitizer to capture the analog readback wave forms for the SNR signal processing. For more accuracy, the readback wave forms are then up-sampled to ten samples per bit.

In spin-stand SNR measurement, 50 periods of a 255-bit-long pseudorandom bit sequence (PRBS) are continuously written in the first sector. To decouple media noise from the noise induced by the read head, each sequence is read back 50 times. Then, all readback wave forms are realigned using the PRBS autocorrelation property [11] to remove asynchronous reading. After the alignment, all 50 readback wave forms are then averaged to obtain a reading-noise-free wave form that is called the spatially noisy signal. The reader noise can be calculated by subtracting a spatially noisy signal and each 50 aligned readback wave forms. However, the reader noise is not considered in this paper because the simulation does not have the noise contribution from the read head. To acquire the noise-free signal, 50 periods of PRBS signal are extracted from a spatially noisy signal and all 50 spatially noisy PRBS periods are then averaged to obtain the noise-free signal. The spatial noise is calculated from the difference between the noise-free signal and each chopped spatially noisy signal. From the wave-form-averaging method, we obtain the signal power from the noise-free signal, the spatial noise power from the spatial noise, and the time-random noise power from reader noise. The spatial noise can be split into the transition noise and the remanence noise using a proper mask function. The transition noise can be extracted from the spatial noise using a proper mask function, where the transition mask function is nonzero in the transition regions and zero otherwise [8]. The remanence noise can also be calculated by the same method, using an inverted transition mask function. Finally, we can determine the transition and remanence noise powers from the extracted transition noise and remanence noise.

III. IN-HOUSE EXTRACTION OF SNR

The SNR obtained from simulations does not contain contributions arising from the reader. Here, only the magnetic contribution to the noise is considered. The noise from the reader could easily be removed by performing multiple readings of the same track and extracting an average readback signal, as described in Sec. II. To extract the SNR components, we follow a procedure analogous to the experimental one described in Sec. II:

(1) Initially, a wave form is written multiple times on a track with a different random seed to ensure that all writings are independent.

(2) Each track is read back only once, since the noise contribution from the reader is not yet accounted for in our model. The readback model utilized here is detailed in Sec. IV.

(3) Similarly to the experimental approach, the cross-correlation among the individual signals is calculated to eliminate the system asynchronous noise [11,12] caused by the reading and writing of the sequence at different times or locations. The calculation of the cross-correlation is performed in the frequency domain to simplify the calculation, as it involves only multiplication. Eventual time lags and/or phase shifts resulting from the cross-correlation analysis are then subtracted and the sequences are aligned. It is worth mentioning that in the case of our simulations, we expect this contribution to be minimal, since there is jitter due to the writer or reader but only thermal effects during the writing process.

(4) The individual signals are smoothed by applying a low-pass filter to remove the highest component in the frequency spectrum, where the cutoff frequency is determined from the frequency of the shortest bit pattern written, as described in Ref. [13]. Subsequently, the average signal, defined as the noise-free signal [7,8], is computed by averaging spatially over each signal. The smoothed signals (blue), their average (red), and the magnetization configuration of one of the written tracks are plotted in Figs. 1(b) and 1(a), respectively.

(5) The average signal variance associated with the deviation of the signal from the mean value is calculated, as shown in Fig. 1(c), and it represents the total spatial noise.

(6) The transition and remanence noise are obtained from the total spatial noise by the application of appropriate windowing functions. For transition noise, a windowing function that is nonzero only around transitions is chosen, while for remanence noise, we choose a function that goes to zero close to transitions. The resulting noises are depicted in Figs. 2(b) and 2(c), respectively. In both cases, the blue line represents the spatial noise given by the signal variance, i.e., the same as plotted in Fig. 1(c).

(7) The SNR for each of the noise components is calculated from the power definition: $\mathrm{SNR}_{\mathrm{dB}} = 10 \log_{10} \left(P_{\mathrm{signal}}/P_{\mathrm{noise}} \right)$. The power is obtained as the area under the signal-to-noise curves, where for transition and remanence noise, the windowing is applied to the noise only, since we are interested in the effect of each individual component on the total signal power.
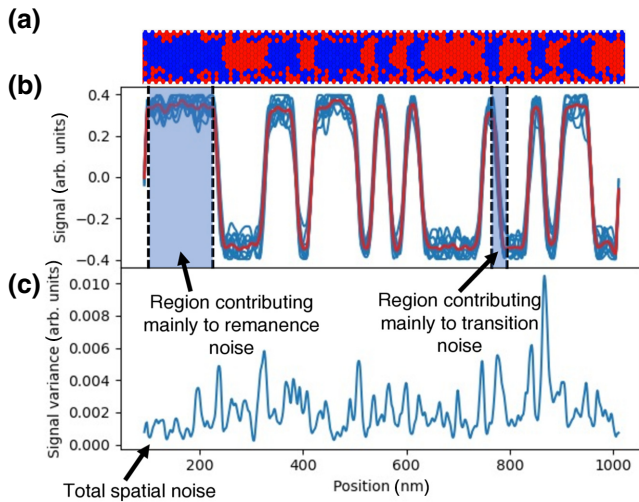
FIG. 1. (a) A snapshot showing the magnetization of the grains after the PRBS is written for a specific random seed. The palette gives the z component of the magnetization ($z = -1$ red, $z = +1$ blue) and the extra initial 00 and final 11 bits are not plotted. (b) The readback signals (blue) and their average (red) as a function of the down-track position, which is the same as for the snapshot in (a). The two shadowed areas exemplify the remanence and transition contributions to the noise. (c) The signal variance, i.e., the total spatial noise, as a function of the down-track position.

Next, we consider the SNR of the HAMR writing process with different maximum temperatures and make a direct comparison between the SNR components extracted from simulated data obtained by our in-house software and the Seagate proprietary software, as demonstrated in Fig. 3,
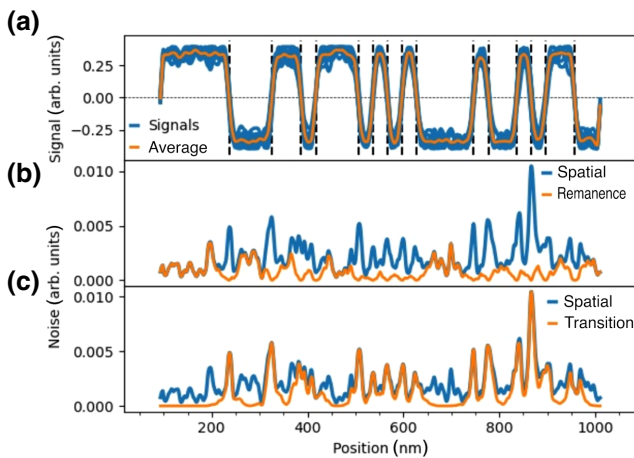

FIG. 2. (a) The down-track profile of the individual signals (blue) and their average (orange), where the dashed vertical lines mark the transition locations. (b) The remanence noise (orange), obtained by windowing the spatial noise, i.e., the total signal variance (blue), as a function of the down-track position. (c) The transition noise (orange), obtained by windowing the spatial noise, i.e., the total signal variance (blue), as a function of the down-track position.
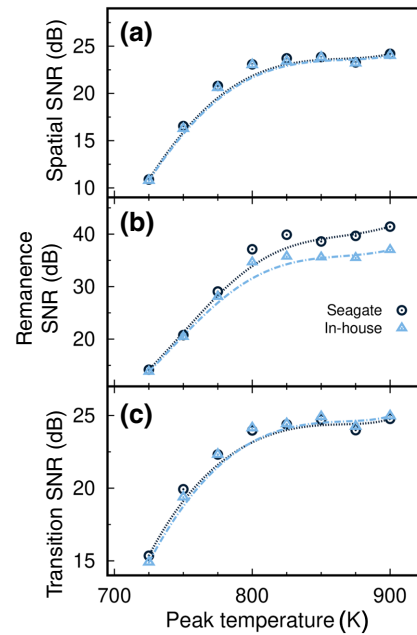

FIG. 3. A comparison of the different signal-to-noise ratio (SNR) components as a function of the maximum temperature of the temperature profile between our in-house results (light-blue triangles) and the Seagate software (black dots). The lines are a guide to the eye.

to confirm the agreement and validity of our in-house software. In this case, the pattern is the 31-bit-long PRBS 1111100011011101010000100101100, obtained from the polynomial $x^5 + x^3 + 1$, where in this notation, a 1 represents a down bit (magnetization along the negative z axis) and a 0 represents an up bit (magnetization along the positive z axis). The written sequence includes extra initial 00 and final 11 bits to ensure that the PRBS is written properly; these are then excluded from the analysis. The sequence is repeated 20 times to give reasonable statistics. It can be noted that the results agree very well for spatial and transition SNR, whereas we do observe some discrepancies for transition SNR as the temperature increases. At such temperatures, the remanence SNR is 30 dB or higher and the magnetization signal is clean in the remanence regions, with hardly any noise. There are, however, differences in the analytical approaches in the way the signal is cut, and this truncation process may affect the computation of the noise, resulting in a different value for the SNR. However, since SNR values of 30 dB are unlikely in realistic media, we can neglect the difference and consider the agreement satisfactory. Thus, in the following, we present SNR data obtained by our in-house software.

As already detailed in our previous work [9], to accurately determine the SNR, a large number of total bits is required. Figure 12 of Ref. [9] shows the SNR as a function of the total number of simulated bits. There, it can be seen that the SNR converges as the number of total bits is

increased, with maximum fluctuations of the order of 0.05 dB for 5000 bits or more.

IV. SIMULATIONS

To describe and simulate the magnetization dynamics of a HAMR magnetic medium, we utilize MARS [9], an open-source multi-time-scale micromagnetic code designed for the modeling of advanced recording systems, where each grain is treated as an individual macrospin of magnetization $\vec{M}$. Since HAMRs involve heating the medium up or close to the Curie temperature (T_c) of the magnetic film, the approach is based on the integration of the Landau-Lifshitz-Bloch (LLB) equation [9]:

$$
\frac{\partial \vec{m}^i}{\partial t} = -\gamma \left(\vec{m}^i \times \vec{H}_{eff}^i \right) + \frac{\gamma \alpha_{\parallel}}{m^{i2}} \left(\vec{m}^i \cdot \vec{H}_{eff}^i \right)
$$
$$
- \frac{\gamma \alpha_{\perp}}{m^{i2}} \left[\vec{m}^i \times \left(\vec{m}^i \times \left(\vec{H}_{eff}^i + \vec{\zeta}_{\perp}^i \right) \right) \right] + \vec{\zeta}_{ad}^i. \quad (1)
$$

Here, $\vec{m}_i = \vec{M}^i / M_s{}^i$ and m_i are the reduced magnetization and magnetization length of the ith grain, γ_e is the electron gyromagnetic ratio, and $\vec{H}_{eff}^i$ is the effective field acting on grain i. $\alpha_{\parallel}$ and $\alpha_{\parallel}$ are the longitudinal and transverse components of the damping and depend on the phenomenological Gilbert-damping parameter λ. $\vec{\zeta}_{\perp}^i$ and $\vec{\zeta}_{ad}^i$ are the diffusion coefficients of grain i, which describe the finite-temperature effects on the perpendicular and parallel components of the magnetization, respectively. The effective field includes the contributions from the longitudinal relaxation of the magnetization, the external applied field, and the intragrain exchange field. The latter is a term of an atomistic nature that accounts for the decrease in length of the magnetization at finite temperature, which is fundamental when describing processes such as those involved in HAMR.

In HAMR technology, the medium is heated up by an extremely narrowly focused beam to temperatures close to
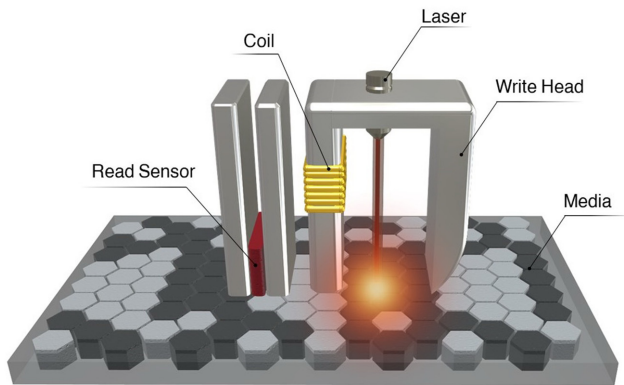

FIG. 4. A schematic of the writing process in HAMR technology (courtesy of W. Pantasri).

T_c in order to reduce the anisotropy of the grains and hence to be able to switch the magnetization of the grains at lower external fields, as illustrated in Fig. 4.

In our model, we describe a HAMR process as a continuous laser recording process, where the laser is switched on during the whole writing time and the direction of the external magnetic field H_{app} is reversed from the previous orientation when a transition needs to be recorded. Assuming that the medium spins along the down-track (x) direction with velocity $v = -v_{head}$, the temperature profile has a Gaussian profile and can be expressed as

$$
T(x, y, t) = T_{amb} + \left[T_{peak} - T_{amb} \right] T(x, t) T(y),
$$
$$
T(x, t) = \exp \left[-\frac{(x - vt)^2}{2\sigma_x^2} \right], \quad (2)
$$
$$
T(y) = \exp \left[-\frac{(y - C_y)^2}{2\sigma_y^2} \right],
$$

where $T(x, t)$ and $T(y)$ are the profiles along the down-track and cross-track (y) directions, respectively, T_{amb} is the temperature of the system when the laser is off, and T_{peak} is the maximum temperature reached during the heating. $\sigma_{x,y} = \text{FWHM}_{x,y} / \sqrt{8 \ln 2}$ is the standard deviation of a Gaussian profile with full width at half maximum $\text{FWHM}_{x,y}$ and C_y is the center of the write head in the cross-track direction. H_{app} has a trapezoidal time profile and is applied uniformly beneath the writing head with a magnitude that switches sign when the polarity is reversed:

$$
H_{app} = \begin{cases} H_{min} + \left(\frac{H_{max} - H_{min}}{t_{ramp}} \right), & \text{ramp up,} \\ H_{max} - \left(\frac{H_{max} - H_{min}}{t_{ramp}} \right), & \text{ramp down,} \\ H_{max} \text{ or } H_{min}, & \text{between ramps.} \end{cases} \quad (3)
$$

To perform the read back, the system is first discretized into 1 nm^2 cells with the read head set on the center of the track. The read head is then moved along the track in single-cell increments, with the magnetization determined via the average magnetization within the read head at each step. This reading process models an ideal read head. This means that we assume the reader is able to read the magnetization pattern without any loss. It follows that the simulated readback signal is higher than the respective readback signal measured experimentally, as there are no thermal effects, effects due to mispositioning of the reader, loss of sensitivity at the edges, and/or other disturbances.

A detailed and exhaustive description of the HAMR model and the code functioning can be found in Ref. [9].

A. Material parameters

The magnetic properties of the medium utilized in the spin-stand tests are unknown and a generic Fe-Pt granular

TABLE I.   The simulation parameters for the systems investigated.

Parameter	Value	Units
Curie temperature T_c	700	K
Curie temperature distribution σ_{Tc}	0.03	
Magnetic anisotropy K_u	4.2	MJ/m^3
Anisotropy field distribution σ_{Hk}	0.15	
Saturation magnetization M_s	1.05	MJ/(m^{3}T)
Gilbert damping λ	0.05	
Average grain diameter	6	nm
Grain thickness	8	nm
Grain volume distribution σ_D	0.15	

TABLE II.   The parameters for the HAMR simulations.

Parameter	Value	Units
System width	100	nm
Bit length BL	16	nm
Track width TW	50	nm
Heated-spot FWHM$_x$	100	nm
Heated-spot FWHM$_y$	70	nm
Read-head velocity v_{head}	22	m/s
Skew angle	0	°
Field ramp time t_{ramp}	100	ps
NFT-to-pole spacing NPS	Small, medium	

film is assumed. The film is built as a Voronoi tessellation with grains of average diameter 6 nm and a thickness of 8 nm. The Fe-Pt grains are characterized by the following zero-temperature parameters: saturation magnetization, $M_s = 1.05$ MJ/(m^{3}T); anisotropy energy density, $K_u = 4.2$ MJ/m^3; and Gilbert damping, $\lambda = 0.05$. We perform atomistic simulation by means of the atomistic spin package VAMPIRE [14] to determine the input parameters required by MARS in order to describe the system accurately [9,15]. We consider 15% distribution in the grain volume (σ_D), 15% in the anisotropy field (σ_{Hk}) and a 3% distribution in $T_c(\sigma_{Tc})$, values often reported in the literature for realistic HAMR media [2]. We limit our investigation to a H_{app} of 0.8, 1 T aligned along the perpendicular direction to the magnetic film, and we vary the maximum of the temperature profile T_{peak} from 700 to 900 K, a temperature range that covers operations from just above T_c to about 200 K above the T_c of Fe-Pt. However, since the results do not differ appreciably, we only show those for $H_{app} = 1$ T. These parameters are summarized in Table I

B. Setup parameters

The writing process depends on the properties and setup of the write head other than the medium properties. Among these, there are the maximum temperature reached by the laser when it hits the medium, generated by the near-field transducer (NFT), the distance between the NFT and the coil that generates the magnetic field, defined as the NFT-to-pole spacing (NPS), and the strength of the magnetic field generated by the coil. Thus, to investigate the noise in HAMR media due to the write head, we apply different NFT peak temperatures. We also consider different HAMR heads characterized by different NPS values: these are confidential and thus are defined in the following as small and medium NPS. The parameters for the writing process are set to agree with those utilized in the spin-stand tests described in Sec. II, to allow a direct comparison between the simulations and the experimental data. The experimental revolution speed is 7200 rpm with a 1.1-in. radius at a

frequency of 1.47 GHz, corresponding to a bit length (BL) of approximately 16 nm, a track width (TW) of 50 nm, and a linear velocity $v_{head} = 22$ m/s, with a 0° skew angle. The applied field has a ramp time (t_{ramp}) of 100 ps. To obtain similar values of BL and TW in our simulations, we set the heated-spot FWHM in the down-track and cross-track directions (FWHM$_{x,y}$) to 100 nm and 70 nm, respectively. It is important to observe that in case of nonzero NPS, a larger spot size and a higher maximum temperature of the heat profile than commonly assumed [5,16,17], as in this work, are necessary. The reason lies in the necessity of reaching the same temperature in the region where the external field is applied. The parameters describing the experimental setup are summarized in Table II

To be able to compare the simulation results with the experimental data, we extract the T_c of the film by performing thermal-erasure simulations on the same system, in analogy to the spin-stand protocol performed by Seagate and described in Ref. [10]. The thermal-erasure procedure is performed *in situ* and it is a test in which a single-tone track is first written and then an attempt to erase it by having the write head applying heat only is performed. The experiment is repeated multiple times by varying the laser current while keeping the coil current turned off. The laser current is the current that governs the laser power, so that a larger current corresponds to a higher temperature applied to the medium. The temperature associated with the laser current is defined as the write temperature, T_{write}. The coil current is instead the current required to generate the magnetic field and it relates to the magnitude of the applied field. According to Ref. [10], the laser current at which the original signal amplitude is halved, via the appropriate transformation from current to temperature, gives the T_c of the medium. We point out that this obtained T_c is usually higher than the T_c of the single grain.

V. RESULTS

The bit sequences written during the experimental test are 255 bits long. Writing these long sequences may prove a taxing computational task and hence it might be desirable to reduce the computational effort by considering shorter

sequences. To achieve high total-bit numbers, one can simulate multiple systems with fewer bits; however, the smaller the system, the greater is the total number of required simulations. When doing so, one also needs to be aware of the fact that this might lead to reduction of the SNR due to the cross-correlation between bits and it also appears in the form of aliasing in the dibit response, where the dibit response is the cross-correlation between the input wave form and the readback magnetic signal. To confirm this, we simulate three different bit-sequence lengths: 31 (PRBS-31), 63 (PRBS-63), and 127 (PRBS-127). We repeat each writing 100 times for the 31-bit-long sequence and 20 times each for the 63- and 127-bit-long sequences, for the sake of time. We expect the results for PRBS-63 to be less accurate than the others, due to the lower total number of bits considered in the analysis. As such, the SNR of PRBS-63 should be higher than that for PRBS-127, instead of lying in between the results for PRBS-31 and PRBS-127.

The three PRBS are [11111000110111010100001001 01100], [1111010001110010010110111011001101010111 11100000 100001100010100], and [111110100001110 00 10010011011 010110111101100011010010101110111 0011 0010101011111111 000000010000011000010100010111 1001 0001011001110101 00] and are generated from the polynomials $x^5 + x^3 + 1$, $x^6 + x^5 + 1$, and $x^7 + x^6 + 1$, respectively. In this notation, a 1 represents a down bit (magnetization along the negative z axis) and a 0 represents an up bit (magnetization along the positive z axis). We also add extra initial 00 and final 11 bits to the bit sequences, to ensure that the PRBS is well written and that the relevant signal can be properly selected by synchronizing and locating the beginning and end of the sequence. BL and v_{head} are set to agree with the experimental setup, as well as NPS.

The simulation protocol adopted in this study is as follows. The system is initialized with the grain magnetization randomly oriented along either $+z$ or $-z$ and is allowed to equilibrate at room temperature. Subsequently, the writing process starts, with the laser turned on the whole time, moving at velocity v_{head}, and the magnetic field generated by the write head switching polarity according to the input bit sequence. To ensure that the whole track is properly written, the write-head positioning is outside the beginning of the track; similarly, the write head moves out of the track completely before the conclusion of the simulation. In this way, we can ensure that the first and last bits are well written.

A. Magnetization footprint

In Figs. 5(a) and 5(b), we show the average z component of the magnetization over 100 repetitions for PRBS-31, for small and medium NPS, respectively. The four different magnetic configurations per panel correspond to four different maximum writing temperatures, ranging from 700 to 900 K going from top to bottom. For PRBS-31, the average is performed over 100 repetitions to ensure, as discussed above, that a large number of bits is written and the SNR can be determined accurately. We also highlight the fact that the two initial and final bits are the extra 00 and 11 bits, written to ensure that the desired sequence can be properly determined. We find good agreement with the experimentally determined reconstructed magnetization footprints for HAMR [18,19], with, in particular, similar bit curvature. We can observe how the track turns out to be well defined and measures 50 nm, as for the experimental data. The latter is mainly determined by the revolution speed, FWHM$_y$, and the H_{ani} of Fe-Pt, whereas the well-defined track edges can be ascribed to the 100 repetitions of the writing process We also measure an average BL of 16 nm, which is also in agreement with the provided experimental data. It emerges clearly how the transitions between bits—and, in particular, dibit transitions—are better defined as T_{peak} increases (going from the top to the bottom of each panel). This is something that we can expect, since a higher temperature further reduces H_{ani} and also increases the spot size for the same FWHM$_y$. This suggests that a higher laser power is beneficial for the writing quality; however, an increase of the laser power makes the device more energy inefficient. Moreover, if it is true that transitions are better written by increasing FWHM$_y$, this also comports, for larger and larger laser powers, an increase in the track width and consequently a reduction in the areal density. Thus a trade-off must be reached in order to maximize the efficiency of the writing process and the areal density. Another feature that emerges is the shift of the written pattern further away from the down-track position, marked by 0 nm as the NPS increases. The heat demagnetizes or greatly reduces the M_{s} and K_{u} of the grains, but is the external field to determine the final state of the grain magnetization. Since in our model we keep the NFT position constant and translate the field region, this results in a "delay" of the written pattern. However, we would like to emphasize that this is an intrinsic effect: in fact if, as reference position, the field region were to be taken, we would simply be assisting in producing an opposite shift. Of course, in real devices this is accounted for and corrected to ensure that bits are written in the correct region. The width of the heat spot in the down-track position is governed by the FWHM$_x$ parameter. Clearly, from our results it can be seen how, for the temperature ranges investigated here, the chosen FWHM$_x$ allows us to write bit sequences even for larger values of NPS. However, it is likely that the design properties of the write heads differ slightly for different values of NPS. As is discussed later, this might also impact the SNR.

In in Figs. 5(a) and 5(b), we show the first 600 nm of the average z component of the magnetization computed over 20 repetitions for the PRBS-127 for small and medium
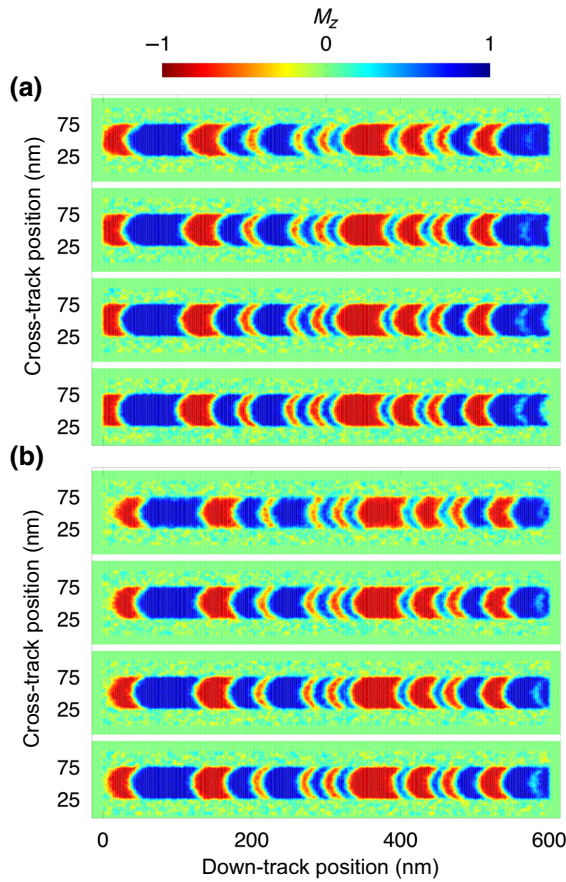
FIG. 5. The average out-of-plane magnetic configuration of the written PRBS-31 for (a) small and (b) medium NPS ($z = -1$ red, $z = +1$ blue). In each panel, the maximum temperature of the temperature profile increases going from top to bottom.

NPS, respectively. The fact that we show only a portion of the bit sequence does not affect the analysis; instead, it helps in making the visualization clearer. Moreover, here we do not present the magnetization configuration for PRBS-63, as the same number of repetitions have been performed. All three PRBSs are considered when discussing the SNR. We first note the lower definition of the tracked edges in comparison to Fig. 5. This is caused by the fewer writing repetitions performed for the longer sequence, for the sake of computational time. Nonetheless, the average track width can still be measured and it respects the target 50 nm. The same holds for the transitions, where despite the worse definition, they can still be located and analyzed. As observed in Fig. 5, as T_{peak} increases, the bit regions become more defined both in the down-track and the cross-track directions. In addition, by inspection, we could expect a larger noise from patterns written only 20 times. However, as we discuss in the following, this does not occur.

B. SNR

In Fig. 7, we present a comparison between the SNR obtained experimentally from spin-stand measurements and the SNR extracted from simulations of HAMR dynamics with MARS, the same as shown in Figs. 5 and 6. We show the comparison for all the three PRBS investigated in Figs. 7(a), 7(b), and 7(c) as a function of the write temperature T_{write}, normalized with respect to the T_c of the film, described in Sec. IV B. The error bars characterizing the experimental data come from the average over different heads with the same NPS. We also point out that the experimental data are the same in all three panels. In high-density media, transition noise is expected to be the dominant source of magnetic noise, since there are more transitions than regions where the magnetization is uniform. We find confirmation of this in both the simulated data and the experimental results, other than the magnetization snapshots. By comparing the spatial and transition SNRs, we see that they are the lowest and that they are almost the same. There can be different types of transitions
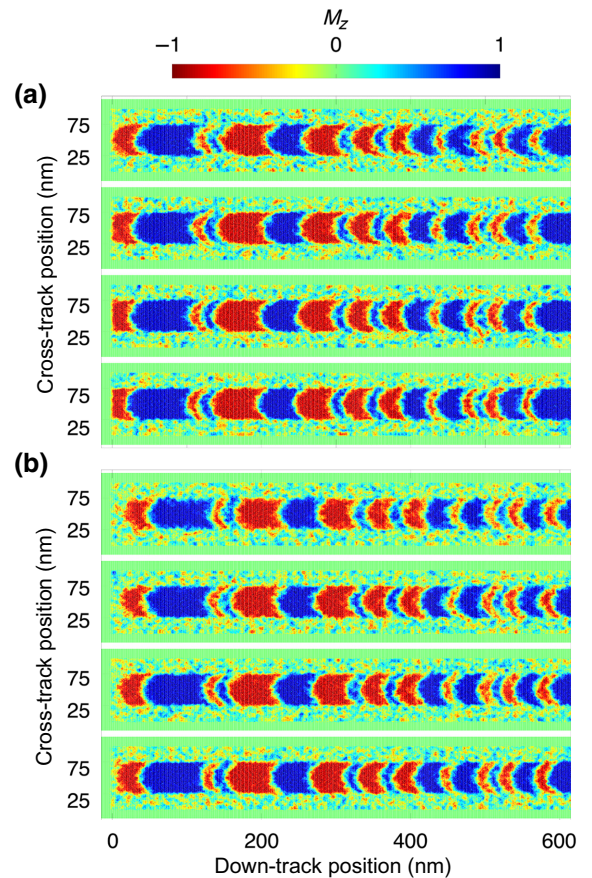

FIG. 6. The average out-of-plane magnetic configuration of the first 600 nm of the written PRBS-127 for (a) small and (b) medium NPS ($z = -1$ red, $z = +1$ blue). In each panel, the maximum temperature of the temperature profile increases going from top to bottom.

in a PRBS to mimic realistic data sets, from the dibit, where there is a single up bit and down bit, to transitions where there are multiple bits that have the same magnetization orientation. The former is the hardest to write and, as such, dominates the transition SNR. We also would like to point out that once the noise is smoothed out, the highest-frequency component left will belong to dibits. On the other hand, a transition between five or more bits having the same polarity will be characterized by lower frequency. Thus, the frequency spectrum of a PRBS generally contains a multitude of frequencies and these can all contribute to the noise.

It emerges from the data, for all three PRBS lengths, that varying the distance between the NFT and the coil does not impact appreciably on the spatial and transition noises, whereas it does affect the remanence component. As the NPS increases, the field is applied to a colder and colder region of the film, i.e., to grains the magnetization and anisotropy of which are recovering. For dibits, where the polarity of the field is rapidly reversed, this means that the field is not applied for a sufficiently long time to successfully reverse all the grains within the bit region. Such an effect strongly depends on v_{head} and T_{peak}. If the writing process is slow, the effect can be mitigated and similar transition SNRs for different NPS can be achieved. However,

realistic revolution speeds, such as the one considered here, involve a fast writing process. The second major factor is the maximum temperature applied on the film. It is simple to imagine that as T_{peak} increases, the heat spot increases and a larger number of grains is demagnetized. It follows that a shift in the position of the NFT becomes more and more negligible. This is what we observe in both the experimental and the simulated results. Interestingly, the experimental results for different NPS values exhibit larger differences in the remanence SNR, which can reach nearly 10 dB in magnitude. As the laser power increases, with T_{write} above 150% of T_c, we observe a tendency to reach similar SNR values. In the SNR obtained from simulations, the difference in the remanence SNR between small and medium NPS is of smaller magnitude and tends to disappear at lower T_{write}, around 120% of the T_c of the film. A likely reason for this different behavior of the remanence SNR is the fact that in building our model, we select the same FWHM$_{x,y}$ parameters for both NPS values. This is not necessarily true for real write heads. Of course, there might also be some differences in the design of heads with different NPS values concerning the type of NFT or the coil. A possible indication of this is the larger error bars in the remanence SNR for the medium NPS; however, in our model these features are not accounted for yet. These
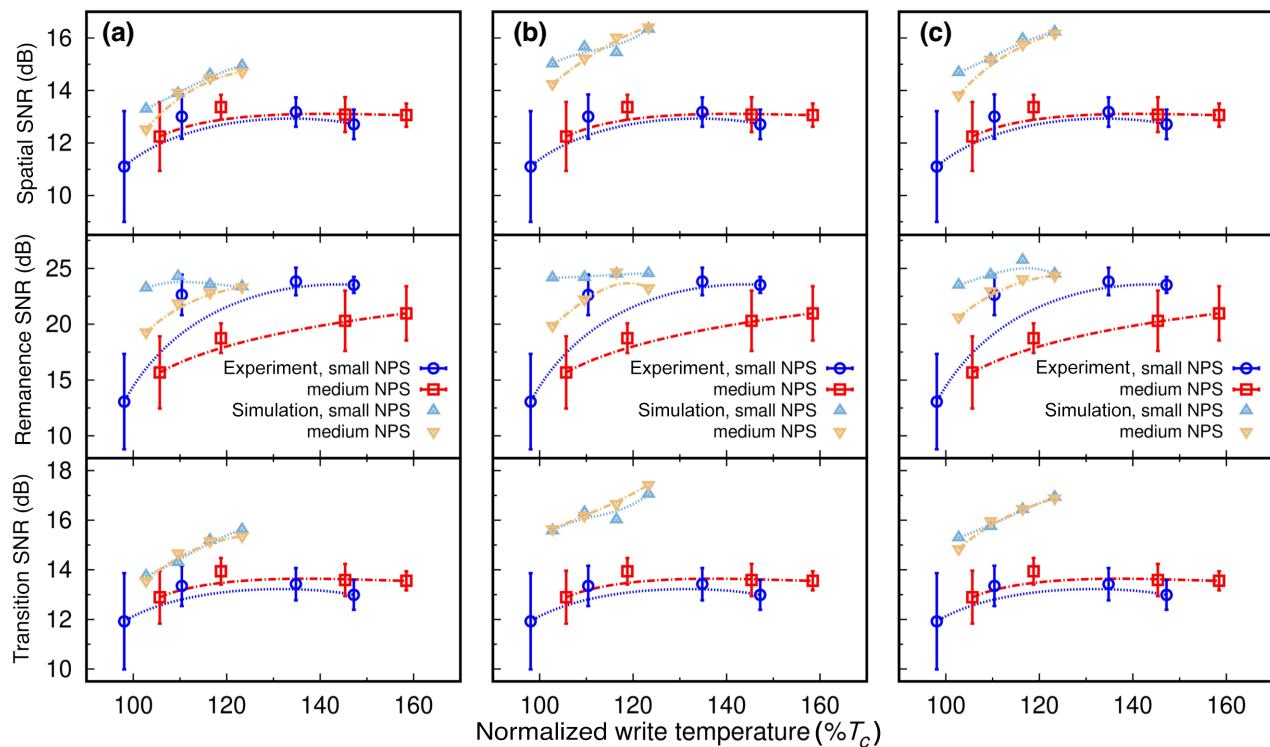

FIG. 7. The different SNR components as a function of the normalized write temperature in units of percentage of medium T_c (%T_c) for differing NFT-to-pole spacing (NPS). The SNR components are the spatial SNR, the remanence SNR, and the transition SNR. The plots compare experiments (dark-blue circles and red squares) with simulations (light-blue triangles and yellow inverted triangles) for (a) 31-, (b) 63-, and (c) 127-bit-long sequences. The lines are a guide to the eye.

factors may be responsible for the discrepancies that we observe.

As mentioned above, we perform a different number of repetitions for PRBS-31 (100) than for PRBS-63 and PRBS-127 (20). The total number of bits (transitions) written is analogous for PRBS-31 and PRBS-127, whereas fewer are written for PRBS-63. We expect that the SNR obtained from the analysis of the 100 repetitions of the shortest bit sequence is the lowest due to the reduced phase space, in this case of transitions, sampled to obtain the average. It may seem surprising that the system that exhibits the highest SNR is the one with fewer repetitions, when comparing the average magnetization profiles for the different bit-sequence lengths in Figs. 5 and 6. This is what we find by inspecting Figs. 7(a) and 7(c), where the trend of the data is the same but there is a downshift of the SNR components in panel Fig. 7(a) for PRBS-31. This is confirmation of the fact that to obtain an accurate estimation of the noise arising from the magnetic medium, it is important to consider different bit patterns and transitions. It is also important, however, to average over a large number of bits and transitions, as already demonstrated in Ref. [9]. It follows naturally that the *hybrid* case of PRBS-63 does not meet these criteria for accuracy. On the one hand, the sequence is longer than PRBS-31 and thus it would allow for less cross-correlation between bits; however, there are fewer bits in total (transition). Because of this, the results presented in panel Fig. 7(b) for PRBS-63 have a higher SNR than PRBS-127 instead of being in between those for PRBS-31 and PRBS-127. We would like to stress that these differences emerge in the SNR analysis, whereas if we were to limit ourselves to the analysis of the average magnetization configurations, we would not find differences between PRBS-63 and PRBS-127 and these would exhibit lower definition than PRBS-31. This also allows us to determine a minimum level of definition for the track and bit edges in order for the track to be considered sufficiently well written.

Overall, we can conclude that the proposed approach is able to simulate realistic writing and reading processes and the SNR analysis agrees with the experimental data even in the absence of complete knowledge of the experimental system and setup.

VI. CONCLUSIONS

We develop a code to extract the SNR arising from the magnetic film in a recording medium. The approach allows us to separate the remanence and transition contributions from the global spatial noise. The results are in excellent agreement with the analysis performed on the same data sets using the proprietary Seagate software based on ensemble wave-form analysis.

We also achieve good agreement between the SNR obtained from spin-stand measurements on a nonspecified Fe-Pt medium and the SNR extracted from simulated HAMR dynamics via a LLB-based granular model. This demonstrates the capabilities of the approach to reproduce the main features and properties of the HAMR process. It also shows how this overall approach could prove to be a useful tool to assist the development of future HAMR technology if state-of-the-art parameters and inputs are provided.

[1] Y. Jiao, Y. Wang, and R. H. Victora, A study of SNR and BER in heat-assisted magnetic recording, IEEE Trans. Magn. **51**, 1 (2015).

[2] D. Weller, G. Parker, O. Mosendz, A. Lyberatos, D. Mitin, N. Y. Safonova, and M. Albrecht, Review article: FePt heat assisted magnetic recording media, J. Vac. Sci. Technol. B, Nanotechnol. Microelectron.: Mater., Process., Meas., Phenom. **34**, 060801 (2016).

[3] G. Mian and T. Howell, Determining a signal to noise ratio for an arbitrary data sequence by a time domain analysis, IEEE Trans. Magn. **29**, 3999 (1993).

[4] H. Bertram and M. Williams, SNR and density limit estimates: A comparison of longitudinal and perpendicular recording, IEEE Trans. Magn. **36**, 4 (2000).

[5] R. H. Victora and P. W. Huang, Simulation of heat-assisted magnetic recording using renormalized media cells, IEEE Trans. Magn. **49**, 751 (2013).

[6] Kai-Zhong Gao and H. Bertram, Transition jitter estimates in tilted and conventional perpendicular recording media at 1 tb/in^2, IEEE Trans. Magn. **39**, 704 (2003).

[7] S. Hernandez, P. Krivosik, P. W. Huang, W. R. Eppler, T. Rausch, and E. Gage, Parametric comparison of modeled and measured heat-assisted magnetic recording using a common signal-to-noise metric, IEEE Trans. Magn. **52**, 1 (2016).

[8] S. Hernandez, P.-L. Lu, S. Granz, P. Krivosik, P.-W. Huang, W. Eppler, T. Rausch, and E. Gage, Using ensemble waveform analysis to compare heat assisted magnetic recording characteristics of modeled and measured signals, IEEE Trans. Magn. **53**, 1 (2017).

[9] S. Rannala, A. Meo, S. Ruta, W. Pantasri, R. Chantrell, P. Chureemart, and J. Chureemart, Models of advance

recording systems: A multi-timescale micromagnetic code for granular thin film magnetic recording systems, Comput. Phys. Commun. **279**, 108462 (2022).

[10] D. A. Saunders, H. Zhou, C. Rea, and P. Czoschke, Magnetic field strength measurements in heat-assisted magnetic recording, IEEE Trans. Magn. **55**, 8 (2019).

[11] F. MacWilliams and N. Sloane, Pseudo-random sequences and arrays, Proc. IEEE **64**, 1715 (1976).

[12] I. Ozgunes and W. Eppler, Synchronization-free dibit response extraction from PRBS waveforms, IEEE Trans. Magn. **39**, 2225 (2003).

[13] S. Hernandez, Z. Liu, P. Jin, S. D. Granz, P. Krivosik, R. Venkataramani, W. Radich, T. Rausch, J. Dykes, and E. C. Gage, Geometrical scaling limits of heat-assisted magnetic recording, IEEE Trans. Magn. **57**, 1 (2021).

[14] R. F. L. Evans, W. J. Fan, P. Chureemart, T. A. Ostler, M. O. A. Ellis, and R. W. Chantrell, Atomistic spin model simulations of magnetic nanomaterials, J. Phys.: Condens. Matter **26**, 103202 (2014).

[15] A. Meo, W. Pantasri, W. Daeng-am, S. E. Rannala, S. I. Ruta, R. W. Chantrell, P. Chureemart, and J. Chureemart, Magnetization dynamics of granular heat-assisted magnetic recording media by means of a multiscale model, Phys. Rev. B **102**, 174419 (2020).

[16] W.-H. Hsu and R. H. Victora, Micromagnetic study of media noise plateau in heat-assisted magnetic recording, IEEE Trans. Magn. **55**, 1 (2019).

[17] N. A. Natekar and R. H. Victora, Analysis of adjacent track erasure in the HAMR media, IEEE Trans. Magn. **57**, 1 (2021).

[18] M. Cordle, C. Rea, J. Jury, T. Rausch, C. Hardie, E. Gage, and R. H. Victora, Impact of radius and skew angle on areal density in heat assisted magnetic recording hard disk drives, AIP Adv. **8**, 056507 (2018).

[19] I. Gilbert, Z. Liu, D. A. Saunders, W. R. Eppler, C. Rea, and T. Rausch, Characterizing curvature in heat-assisted magnetic recording using spin-stand imaging, IEEE Trans. Magn. **55**, 1 (2019).